# Parameter Dependencies of Early-Stage Tangential Discontinuity-Driven Foreshock Bubbles in Local Hybrid Simulations

**Andrew Vu[1], Terry Z. Liu[2], Hui Zhang[1], Peter Delamere[1]**

[1]Geophysical Institute, University of Alaska Fairbanks, Fairbanks, AK, USA, [2]Department of Earth, Planetary, and Space Sciences, University of California, Los Angeles, Los Angeles, CA, USA

Corresponding Author: Hui Zhang (hzhang14@alaska.edu)

Co-corresponding Author: Terry Z. Liu (terryliuzixu@ucla.edu)

## Key Points

- We use local hybrid simulations to test different foreshock ion distributions and properties on the early formation of foreshock bubbles.
- The shape of the foreshock ion distribution in the perpendicular plane dictates the strength of the current and resulting field variations.
- Foreshock ion densities, thermal speeds, and parallel speeds positively and linearly correlate with foreshock bubble expansion speeds.

## Abstract

Foreshock bubbles (FBs) are significant foreshock transients that can accelerate particles and disturb the magnetosphere-ionosphere system. In the kinetic formation model, foreshock ions interact with the discontinuity by performing partial gyrations to generate currents that change the magnetic field topology around the discontinuity. However, how different foreshock ion properties affect the growth of the field variations is not well understood. Therefore, we use 2-D local hybrid simulations to study the effects of different foreshock ion distributions and properties on the growth of tangential discontinuity (TD)-driven FBs. We discover that for a gyrophase-bunched distribution with an initial phase where the guiding center is on the other side of the TD, the foreshock ions gyrate together across the TD, causing more foreshock ions to cross the TD and

This article has been accepted for publication and undergone full peer review but has not been through the copyediting, typesetting, pagination and proofreading process, which may lead to differences between this version and the Version of Record. Please cite this article as doi: 10.1029/2022JA030815.

leading to a faster expansion of the structure than for a Maxwellian distribution. A ring distribution also yields larger expansion speeds because of the larger projected velocity into the new perpendicular direction. For Maxwellian distributions, there are positive and linear correlations of the FB expansion speeds with the initial foreshock ion densities, thermal speeds, parallel speeds, and sine of the TD magnetic shear angles. These parameter dependencies grow in strength as the structures evolve with time. The foreshock ion distributions and properties that lead to stronger currents produce more significant magnetic field variations and larger expansion speeds. Our study helps quantify the formation and expansion of FBs to forecast their space weather effects and contribution to shock acceleration.

# 1 Introduction

Shocks are the most important particle accelerators in the universe and form when a supersonic flow encounters an obstacle (e.g., Helder et al., 2012; Lee et al., 2012). At Earth, when the magnetic field of the supermagnetosonic solar wind encounters the magnetosphere, a bow shock forms. Where the interplanetary magnetic field (IMF) remains magnetically connected with the bow shock surface, the foreshock region is populated with backstreaming foreshock ions that, together with the earthward solar wind ions, can lead to the observations of transient kinetic phenomena called foreshock transients (see review by Zhang et al., 2022). Some types of foreshock transient events exhibit large plasma and field fluctuations such as foreshock bubbles (FBs) (Omidi et al., 2010, 2020; Turner et al., 2013, 2020; Liu et al., 2015; Wang C. P. et al., 2021a) and hot flow anomalies (HFAs) (Schwartz et al., 1985; Thomsen et al., 1986; Paschmann et al., 1988; Schwartz, 1995; Lucek et al., 2004; Facskó et al., 2008, 2009, 2010; Wang S. et al., 2012; Zhao et al., 2015; Chu et al., 2017; Schwartz et al., 2018). FBs typically exhibit a core of hot, tenuous cores of sunward-directed plasma and grow super-magnetosonically in the upstream direction, resulting in a shock connected upstream of their cores and large spatial sizes of 2-10 $R_E$ (e.g., Facskó et al., 2009, 2010; Liu et al., 2016a; Turner et al., 2020). The significant dynamic pressure perturbations of FBs (and HFAs) can lead to deformations of the bow shock surface upon collision, which propagate through and disturb the magnetosphere (e.g., Sibeck et al., 1999; Jacobsen et al., 2009; Hartinger et al., 2013; Archer et al., 2014, 2015; Wang B. et al., 2020, 2021; Wang C. P. et al., 2020, 2021b). Furthermore, FBs and HFAs have been observed to accelerate particles at the bow

shock (e.g., Kecskeméty et al., 2006; Wilson et al., 2016; Liu et al., 2016b, 2017a, 2017b, 2018, 2019, 2020a; Omidi et al., 2021).

Early hybrid simulations show that FBs can be generated with a rotational discontinuity (RD) convecting towards the bow shock (Omidi et al., 2010). However, in-situ observations (Liu et al., 2015) and 3-D global hybrid simulations (Wang C. P. et al., 2021a) show that FBs can also be driven by tangential discontinuities (TD). Recently, particle-in-cell (PIC) simulations (An et al., 2020) and spacecraft observations from the Magnetospheric Multiscale (MMS) Mission (Liu et al., 2020b) demonstrate a kinetic formation model for FBs. In the model, foreshock ions interact with the driver discontinuity by performing a partial gyration and thereby becoming demagnetized. Electrons remain magnetized, and as a result, a Hall current is produced that changes the magnetic field topology of the discontinuity. These magnetic field variations induce an electric field that causes the structure to expand by driving the cold plasma to **E×B** drift outward away from the core. And the motion of the foreshock ions against the induced electric field (in the solar wind rest frame) provides the energy for the expansion of the structure. In recent hybrid simulations confirming the kinetic formation model, Vu et al. (2022) find that the early formation differences between TD-driven FBs and HFAs are dependent on the relative scales of the foreshock ion gyroradii and the TD thicknesses. This paper, which is a continuation of previous simulation work by Vu et al. (2022), focuses on the effects of differing solar wind and foreshock ion parameters on the early formation of TD-driven FBs.

In this paper, we will use 2-D local hybrid simulations to study the effects of different foreshock ion distributions and varying foreshock ion properties on the early formation of TD-driven FBs. Testing different foreshock ion distributions, we will show how the shape of the foreshock ion distribution in the perpendicular plane affects the formation process. We will also show how the foreshock ion parameters, such as their densities, thermal speeds, and parallel speeds, determine the expansion speeds and compression ratios of the formed shocks/compressional boundaries. Based on these simulation results, a quantitative expansion model of FBs is justified and fitted in the accompanying paper (Liu et al., 2023). In Section 2, we will briefly introduce the hybrid code that was used in Vu et al. (2022). In Section 3.1, we will present the early formation of TD-driven FBs from different foreshock ion distributions. In Section 3.2, we will show the effects of various foreshock ion and solar wind ion parameters on the growth

of TD-driven FBs in their early formations and show how their dependencies evolve with time. In Sections 4 and 5, we will discuss and summarize the findings.

## 2 Method

The 2-D local hybrid simulation used in this paper is a continuation of the hybrid code used by Vu et al. (2022) that uses kinetic ions and fluid electrons, assumes quasi-neutrality, and is non-radiative (Swift, 1995, 1996; Delamere et al., 1999; Delamere, 2006, 2009). The electrons are treated as a massless and charge-neutralizing fluid. The motions of the ion macroparticles are governed by

$$\frac{d\mathbf{v}}{dt} = \mathbf{E} + \mathbf{v}\times\mathbf{B} - \nu(\mathbf{u}_i - \mathbf{u}_e),$$

where $\boldsymbol{E}$ is in units of ion acceleration, $\boldsymbol{B}$ is in units of gyrofrequency, and $\nu$ is the collision frequency between ions and electrons. The electric field is calculated through a combination of the electron momentum equation and Ampere's law

$$\mathbf{E} = -\mathbf{u}_e\times\mathbf{B} - \nu(\mathbf{u}_e - \mathbf{u}_i) = -\left(\mathbf{u}_i - \frac{\nabla\times\mathbf{B}}{\alpha n}\right)\times\mathbf{B} - \nu\frac{\nabla\times\mathbf{B}}{\alpha n},$$

where $\alpha = \mu_0 q^2/m_p$ and $m_p$ is the proton mass. The $\alpha$ parameter is used to scale the ion macro-particle densities to physical values. The magnetic fields are advanced using Faraday's law. Dissipation terms for the ion-electron collisions are included in the particle and field equations to reduce numerical instabilities.

The simulation runs are initialized with an ion plasma beta of 1.0, a simulation box size of 202x402 cells where the dimension of each cell is 0.5 ion gyroradii or solar wind ion inertial lengths, and 400 macroparticles per cell. For the TD in the simulation box with its normal in the z-direction (pointing upwards/downwards), the magnetic field is oriented in the +x direction (pointing to the right) in the bottom half and the +y direction (pointing into the page) in the top half. For cases of different cone angles, the magnetic field configuration includes a $B_y$ component while maintaining the magnetic shear across the TD. For cases of varying TD magnetic shear angles, the magnetic field configuration in the bottom half (foreshock side) of the simulation is maintained. In contrast, the top half is adjusted for the desired magnetic shear across the TD. Open boundary conditions are given at the x and z boundary edges (left and right; top and bottom) and periodic boundary conditions are imposed in the y-direction (in and out of the page). A Maxwellian

beam of solar wind ions is initialized everywhere and continuously injected at the left boundary with a bulk flow speed along the +x direction. At the right boundary, from the center of the TD and below, foreshock ions are injected continuously and travel against the solar wind flow antiparallel to the magnetic field. The local magnetic field directions and total ion bulk flows are considered at each time step to ensure that the newly injected foreshock ions remain field-aligned

Based on spacecraft observations of foreshock ions upstream of the bow shock (e.g., Meziane et al., 2004, Tjulin et al., 2009; Burgess et al., 2012), foreshock ions associated with foreshock transients can behave as gyrophase-bunched and ring beam foreshock ion distributions. Therefore, to test the effects of different foreshock ion distributions on the early formation of TD-driven FBs, we initialize the foreshock ions as a Maxwellian beam distribution, a gyrophase-bunched distribution, and a ring beam distribution. We achieve a gyrophase-bunched distribution by adding a perpendicular component at different phases to a Maxwellian beam distribution and a ring beam distribution by adding a ring speed to a Maxwellian beam distribution. Next, to study the effects of differing foreshock and solar wind ion properties on the early formation of TD-driven FBs in their early stages, we keep a Maxwellian beam distribution and vary the parameters of the foreshock ion density ratios, parallel speeds, and thermal speeds one at a time. We also modify the solar wind bulk flow speeds, the solar wind and foreshock ion bulk flow speeds in proportion, and the TD magnetic shear angles.

# 3 Results

## 3.1 Effects of Foreshock Ion Distributions

In this section, we study the effects of different injected foreshock ion distributions in the perpendicular plane on the early formation of TD-driven foreshock bubbles. Because the magnetic field variations at the TD are due to the foreshock ion generated currents, then different foreshock ion distributions should affect the strength of the currents that develop, and subsequently, how significant the magnetic field variations become.

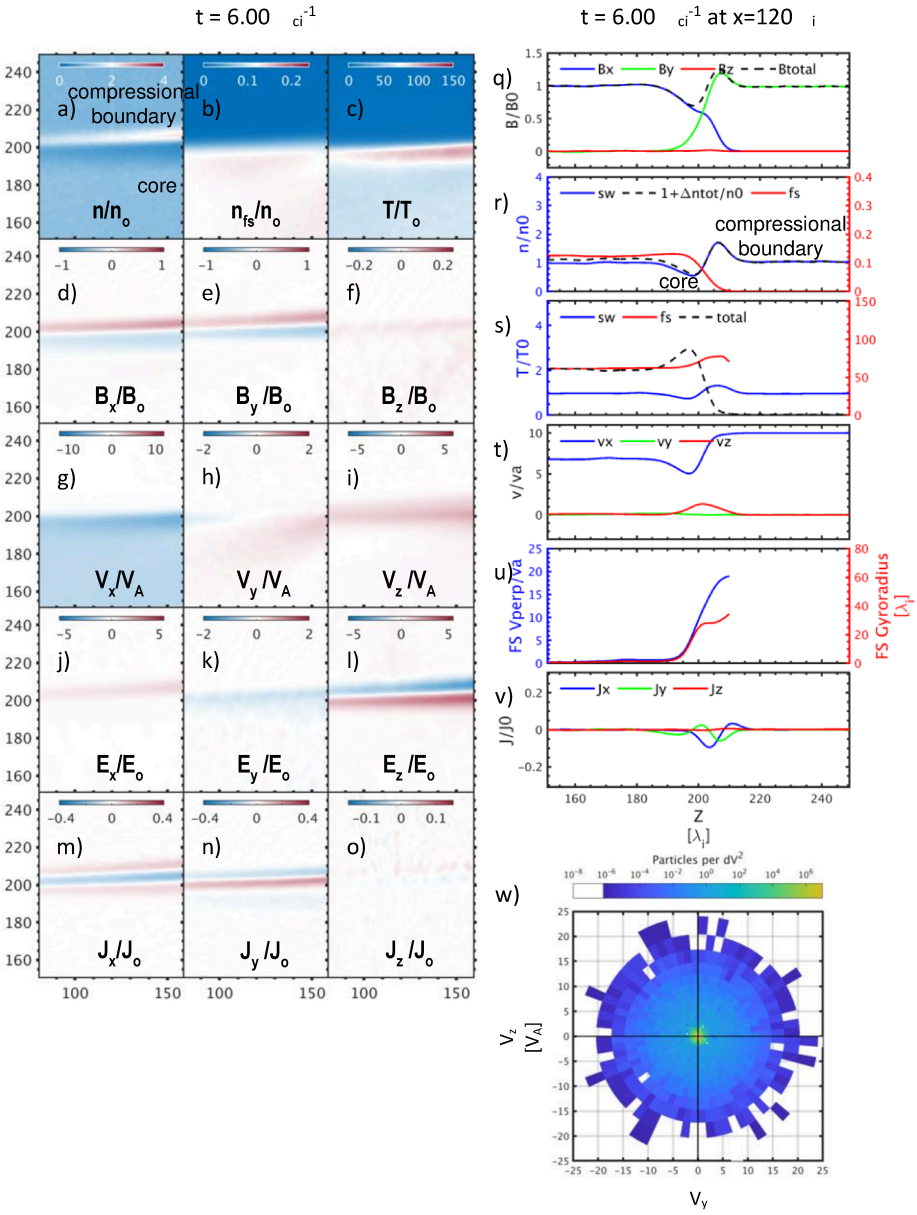

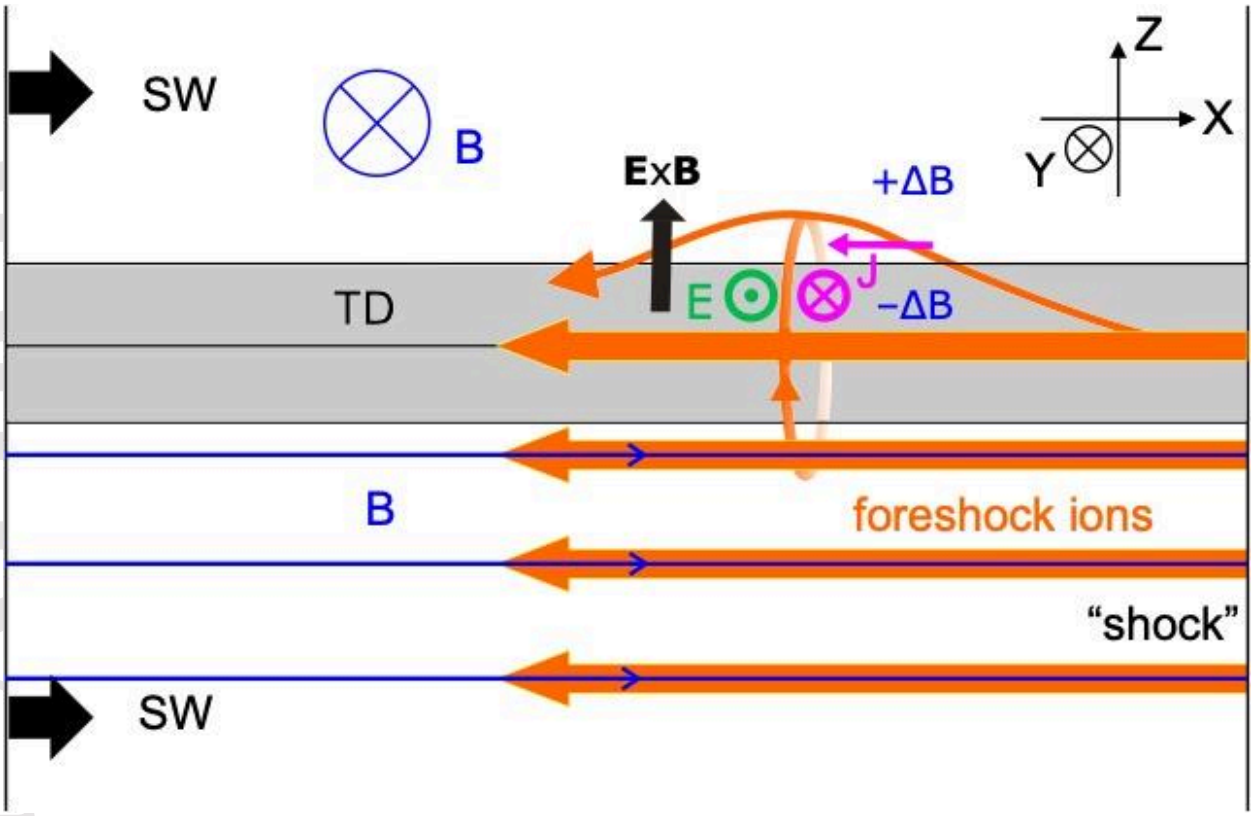


**Figure 1** The top figure shows the results from a case where the foreshock ions are injected as a Maxwellian beam distribution with a thermal speed of 8 $V_A$ (where $V_A$ = 48.95 km/s). Panels a) to o) show the change from the initial time, the 2-D total ion densities, foreshock ion densities, ion temperatures, magnetic field components, ion bulk flow components, electric field components, and current density components. Panels q) to v) show the 1-D magnetic field components and magnitude; solar wind, foreshock, and total ion densities; solar wind, foreshock, and total ion temperatures; total ion bulk flow components; foreshock ion perpendicular speeds and gyroradii; and current density components. The vertical dotted black lines in the 1-D plots mark the positions corresponding to the minimum $J_x$ and the maximum $J_y$ current density components. Panel w) shows the initial ion velocity distribution in the Y-Z plane. The bottom figure shows the simulation setup with an injected foreshock ion beam interacting with a TD of finite thickness. The current direction of the foreshock ion-driven currents is colored as magenta and refers to panels j and k of the 2-D plots. The induced electric field component important for the **E×B** drift (colored as black) of ions, i.e., expansion of the structure, is colored as green and refers to panel h of the 2-D plots. The magnetic field variations due to the foreshock ion-driven currents are labeled in blue and refers to panels d and e of the 2-D plots.

As a point of reference, we begin with Figure 1 with the injection of foreshock ions as a Maxwellian beam with a thermal speed of 8 $V_A$. Figure 1 shows the early formation of a TD-driven FB (consistent with Vu et al. (2022)) at t=6 inverse solar wind ion gyrofrequencies, $\omega_{ci}^{-1}$, with the density depletion and compression in Figure 1a. Figure 1b shows the concentration of foreshock ions within the TD where their initial parallel and perpendicular thermal motion in the –x and +y direction, respectively, projects to a new perpendicular direction as they cross the center of the TD and perform a partial gyration. This thereby leads to the production of foreshock ion-driven currents directed mainly in the –x and +y directions, which tend to decrease the field strength in the core and increase the field strength at the boundary. The solar wind ions, on the other hand, always tend to resist such field variation but cannot overcome it. Thus, the total current in the middle of the FB is determined by the foreshock ion-driven currents, shown by the blue $J_x$ in Figure 1m and by the red $J_y$ in Figure 1n. On two sides of such a current, the red $J_x$ current density regions in Figure 1m and the blue $J_y$ current density regions in Figure 1n are caused by the solar wind ion responses to the field variations; the solar wind ions try to revert the magnetic field variations to their background values and close the current loop. Furthermore, shown in panel k, there is an induced electric field in the –y direction that, together with the $-\Delta B_x$ in panel d, is responsible for driving the cold solar wind ions to **E×B** drift upwards in the +z direction, i.e., causing the expansion of the structure.

Figure 1q shows the variation of the TD magnetic field profile that matches the total density profile in Figure 1r with a tenuous core and a compression boundary. There is an increase in the total ion temperature (dashed black line) within the core due to the presence of foreshock ions. Figure 1t shows a velocity deflection within the core where the foreshock ions are accumulated, and Figure 1v shows the current density component profiles that are driven by the foreshock ions. Figure 1u shows the foreshock ion perpendicular speeds and gyroradii; because the magnetic field within the TD changes in direction and decreases in magnitude, the foreshock ions gain perpendicular bulk speed through velocity projections and larger gyroradii within the TD (because the foreshock ions with larger perpendicular speeds can travel farther upstream away from the TD, there is a dispersion of the perpendicular speeds). Figure 1w shows the initial ion velocity distribution in the Y-Z plane, which is nearly perpendicular to **B** where there is a cold beam solar

wind distribution at the center and a warm foreshock Maxwellian beam distribution at higher thermal velocities.

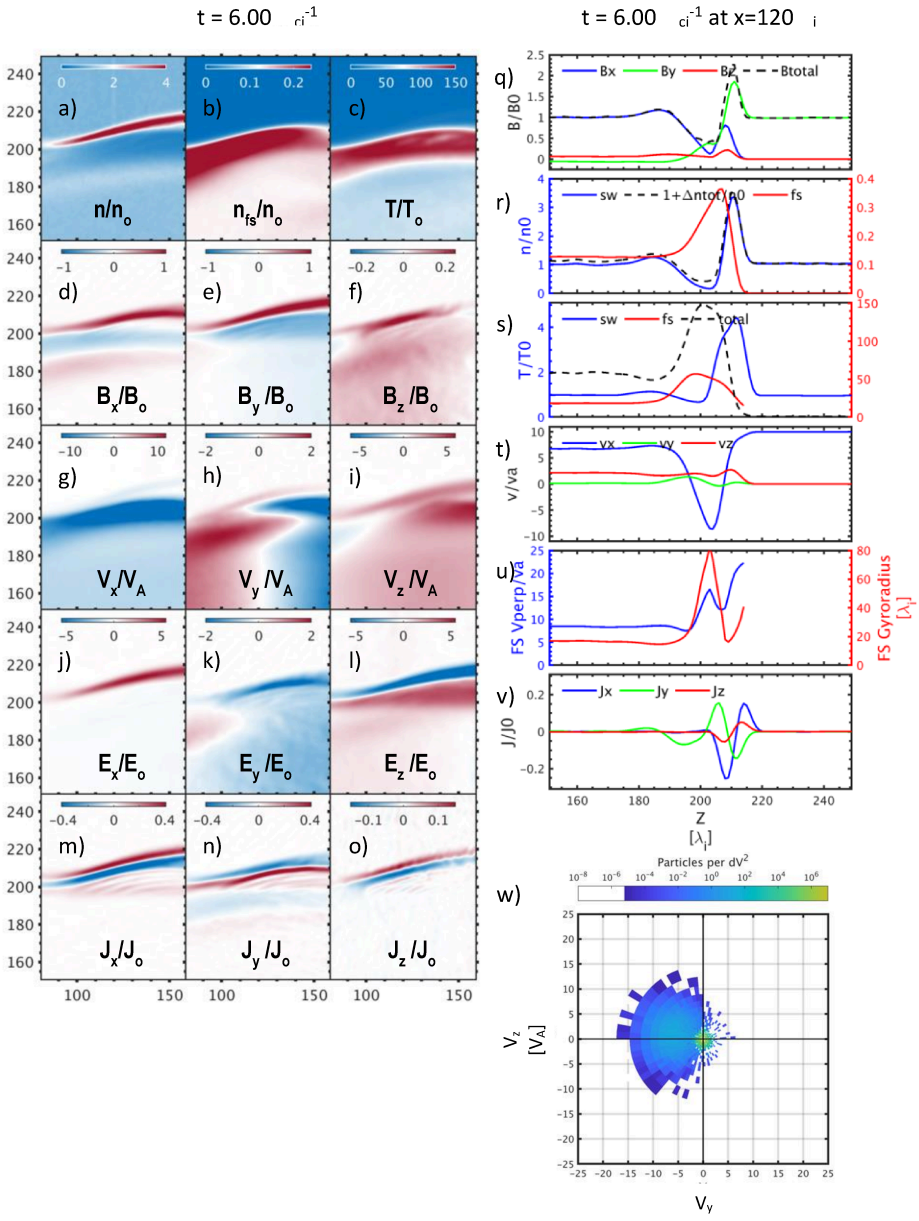

**Figure 2** Results from a case where the foreshock ions are injected as a gyrophase-bunched distribution with a guiding center on the other side of TD and with a thermal speed of 4 $V_A$ and an additional perpendicular bulk speed of 6 $V_A$. The panels follow the format as those in Figure 1.

Deviating from the Maxwellian beam distribution, Figure 2 shows the early formation of the TD-driven FB with the injection of foreshock ions as a gyrophase-bunched distribution with an initial thermal speed of 4 $V_A$ and an additional perpendicular bulk speed of 6 $V_A$ in the −Y direction. Therefore, the total perpendicular energy for the gyrophase-bunched distribution is less than for the Maxwellian beam distribution in Figure 1. In this case (shown in Figure 2w), the gyrophase of the distribution is such that the guiding centers of foreshock ions are on the other side of the TD, therefore, they can gyrate across the center of the TD. The foreshock ions are injected at the same gyrophase at the right boundary in the sketch in Figure 1 and gyrate towards the TD (so when they encounter the TD, they can have a range of gyrophases depending on their initial distance to the TD). Although the gyrophase-bunched distribution is unstable, it has not evolved much during the early stage of formation. Compared to the same time in Figure 1 at t=6 $\omega_{ci}^{-1}$, the TD-directed gyrophase-bunched foreshock ions generate stronger currents (Figures 2m and 2n) than the Maxwellian beam of foreshock ions. This explains the much more significant magnetic field variations in Figures 2d and 2e or Figure 2q, ion depletion and compression in Figure 2a or Figure 2r, and ion flow deflections in Figures 2g and 2i or Figure 2t. This is due to the foreshock ions being initially in the same phase that allows them to gyrate towards the TD together, leading to a higher density of foreshock ions at and across the TD center, which is very apparent in 2-D by Figure 2b or in 1-D by the red line in Figure 2r. The higher density of foreshock ions also corresponds to the total ion temperature's larger increase across the TD in Figure 2c and the black dashed line in Figure 2s. From Figure 2u, the foreshock ions' projected perpendicular speeds are 14 and 13 $V_A$ at the minimum $J_x$ and maximum $J_y$, respectively, which are close to or slightly higher than those in the Maxwellian beam case (15 and 11 $V_A$) in Figure 1u (even though the total perpendicular energy is smaller). Thus, it is the much higher density of foreshock ions that cross the TD that dominates the generation of the larger current and the corresponding stronger structures in this case. Therefore, the distribution shape that determines how many foreshock ions cross the TD is very crucial for the strength of the generated currents.

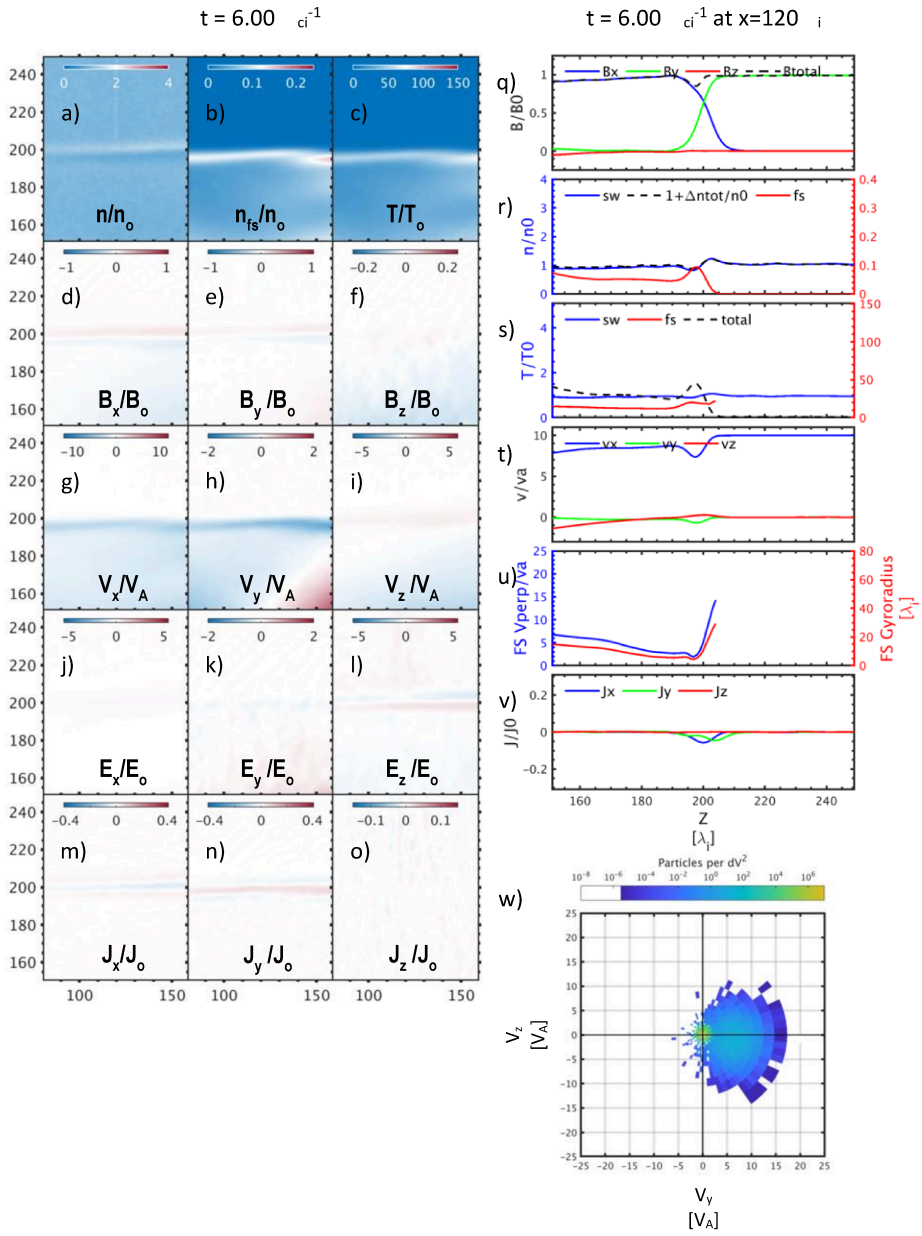


**Figure 3** Results from a case where the foreshock ions are injected as a gyrophase-bunched distribution with a guiding center on the same side away from the TD and with a thermal speed of

4 $V_A$ and an additional perpendicular bulk speed of 6 $V_A$. The panels follow the format as those in Figure 1.

In Figure 3, gyrophase-bunched foreshock ions are injected together in a phase where the guiding centers are on the same side away from the TD (shown in Figure 3w). In this scenario, the foreshock ions can hardly cross the center of the TD (as seen in Figure 3b and the red line in Figure 3r). Thus, there is only a weak current (Figures 3m and 3n or Figure 3v) that is produced to slightly change the magnetic field profile of the TD (Figures 3d and 3e or Figure 3q) and a slight density depletion and compression (Figure 3a or Figure 3r). This further proves the notion that the shape of the distribution is critical to the density of foreshock ions that cross the center of the TD and thus how strong the generated currents are and how strong the magnetic field variations become. We include the results of an intermediate gyrophase in Figure S1 in the Supporting Information.

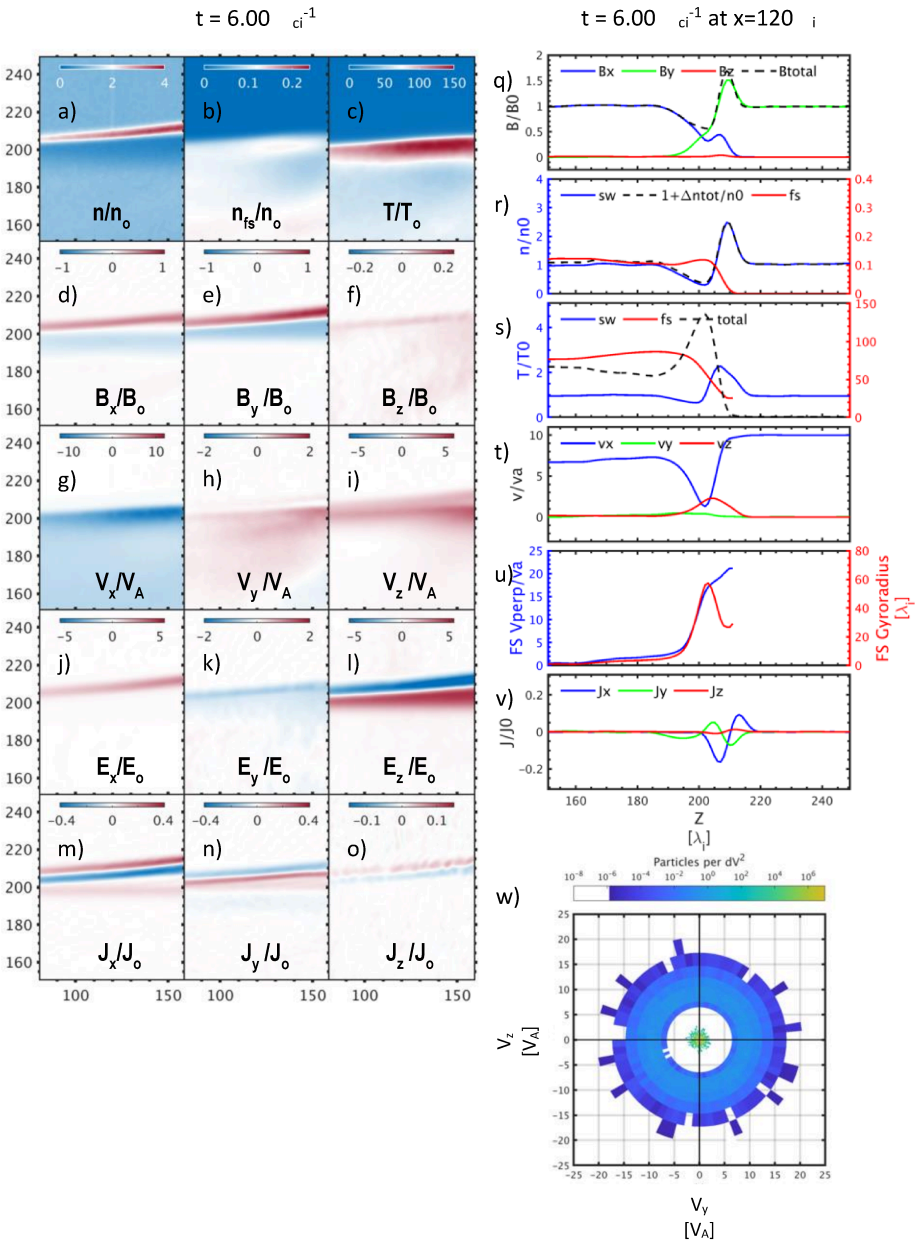

**Figure 4** Results from a case where the foreshock ions are injected as a ring beam distribution with a thermal speed of 4 $V_A$ and a ring speed of $\sqrt{48}$ $V_A$. The panels follow the format as those in Figure 1.

Foreshock ions initially injected as a ring beam, which is common in the Earth's foreshock region, can also lead to faster and more significant growth of the structure. Figure 4 shows the injected foreshock ions as a ring beam distribution with an initial thermal speed of 4 $V_A$ and an additional ring speed of $\sqrt{48}$ $V_A$ (Figure 4w). Although the total perpendicular energy of the foreshock ions in the ring beam distribution is equal to that in the Maxwellian beam distribution, the ring beam case has a more significant density depletion in the core and compression at the boundary in Figure 4a or 4r and magnetic field variations in Figure 4d and 4e or Figure 4q, caused by the stronger generated currents in Figure 4m and 4n or Figure 4v. The stronger foreshock ion-driven currents are due to the higher perpendicular speeds (blue line in Figure 4u) of 24 $V_A$ at the position of minimum $J_x$ and 23 $V_A$ at the position of maximum $J_y$ than the Maxwellian case of 15 and 11 $V_A$ in Figure 1, respectively. With higher perpendicular speeds, foreshock ions possess larger gyroradii (red line in Figure 4u) and can more easily cross the center of the TD and penetrate deeper into the other side of the TD (red line up to z=211 $\lambda_i$ in Figure 4r whereas up to z=208 $\lambda_i$ in Figure 1r). As a result, even though the density of foreshock ions that cross the TD is comparable to that of the Maxwellian beam case (Figure 1r), the larger gyroradii cause a higher total foreshock ion current. We also run a case with a higher ring speed (8 $V_A$), and the foreshock ion perpendicular speeds are even higher, causing stronger currents and more significant structures (Figure S2 in the Supporting Information).

In summary, the shape of the foreshock ion distribution in the perpendicular plane is crucial for the strength of the generated currents because it determines whether and how easily the foreshock ions can cross the TD, and how many of their perpendicular speeds get projected. It is necessary to quantify this in the future to obtain a more general description of arbitrary distribution shapes.

### 3.2 Parameter Dependencies of the Expansion Speed

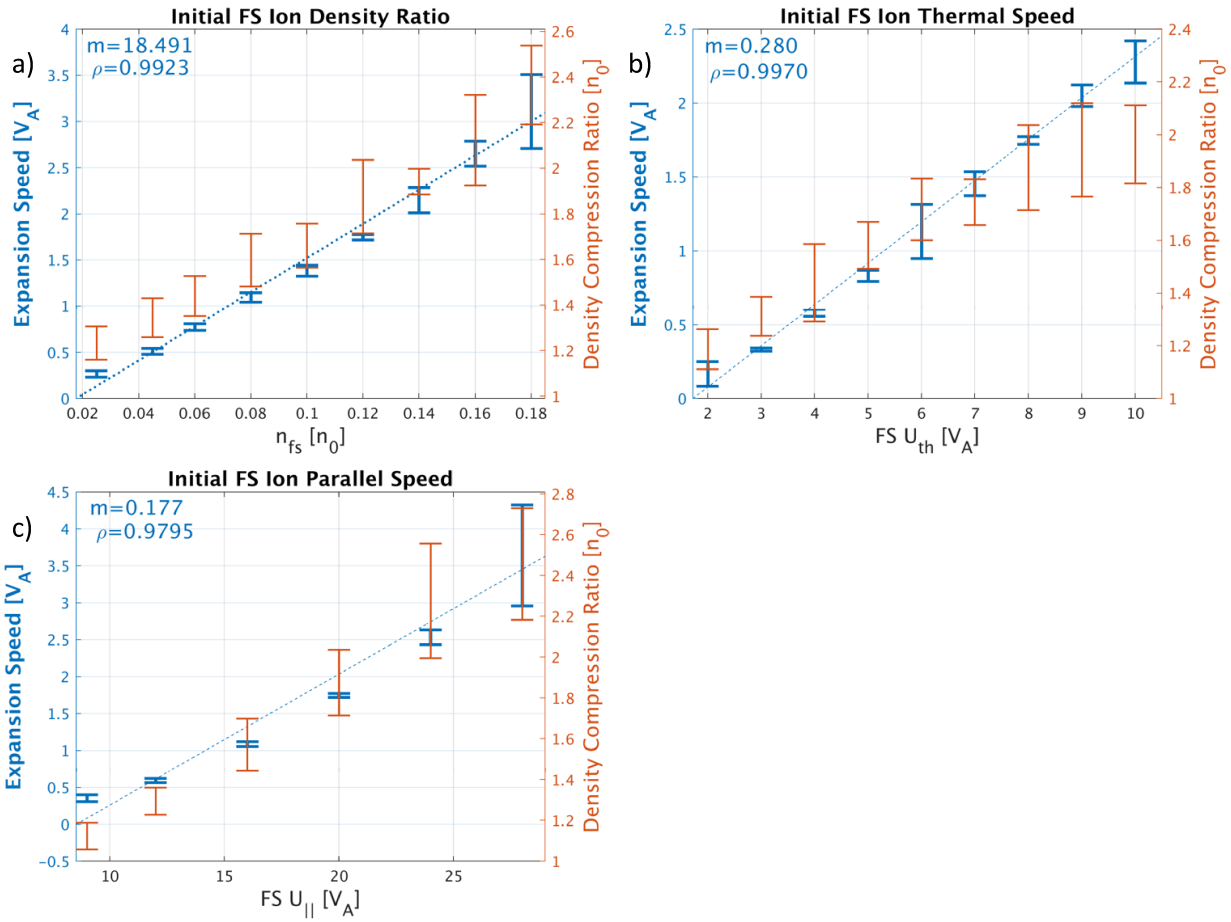


**Figure 5** The foreshock ion parameters' dependencies of the expansion speeds (blue) and density compression ratios (orange) of the compressional boundary at the early stage of formation measured at x=120 $\lambda_i$ and t=6 $\omega_{ci}^{-1}$. Panels a) to c) show the parameters of the initial foreshock ion density ratios, thermal speeds, and parallel speeds. The values in blue at the top left of each panel indicate the fitted slope, m, and correlation coefficient, $\rho$, for each parameter with the expansion speeds. The upper and lower limits of each bar represent the range of the expansion speeds and density compression ratios of adjacent cells along the boundary.

From the various injected foreshock ion distributions, it is apparent that the initial properties of the injected foreshock ions dictate how the structures grow in their early formation. However, testing different foreshock ion distributions is not sufficient in understanding which properties of foreshock ions that influence, and to what extent, the early formation of these structures. Therefore, using a Maxwellian beam distribution for the foreshock ions, we vary, one parameter at a time, the initial foreshock ion densities, thermal, and parallel speeds to see their

effects on the growth of the structures. Although we have not performed the same parameter tests for the other two types of distributions, as their physical processes are essentially the same (e.g., similar current density configurations), the parameter dependencies should be similar and indictive to the other types of distributions.

In the observations, the boundary surface speed or shock speed is commonly used as the expansion speed (e.g., Turner et al., 2020). However, because the simulation output has low time-resolution and because the edge of the weak boundary is very difficult to define during the early formation stage, there are very large uncertainties when we trace the boundary edge to measure its speed. As a proxy, we use the cold solar wind ion bulk flow speed at the compressional boundary in the solar wind rest frame (the **E×B** outward speed) to be the expansion speed of the structure, which is mainly in the +z direction. This speed is slightly slower than the FB shock speed determined by the conservation of mass flux, and we use the ion density compression ratio as a proxy for the FB shock Mach number. Therefore, the FB shock speed of the boundary can be estimated as $v_{shock} \sim \frac{\alpha}{\alpha-1} v_{sheath}$, where $\alpha$ and $v_{sheath}$ are the ion density compression ratio and the ion bulk flow within the boundary, respectively. We show the estimated shock speeds of some FBs in Table 1 of the Discussion.

The results in Figure 5 show the dependencies of the expansion speeds on the foreshock ion density ratios in Figure 5a, the foreshock ion thermal speeds in Figure 5b, and the foreshock ion parallel speeds in Figure 5c. In all three cases, there is a positive and linear correlation of the foreshock ion properties with the expansion speeds (blue) and with the density compression ratios (orange) of the trailing boundaries of TD-driven FBs. The correlation of the density compression ratios is less linear because of the nonlinear relationship between the Mach numbers and compression ratios. To elaborate, higher initial foreshock ion density ratios mean that there will be more foreshock ions that enter the TD to produce stronger currents that will then cause more significant magnetic field variations at the TD. More significant magnetic field variations induce larger electric fields and thus drive cold solar wind ions **E×B** drifts (expand) faster. In other words, stronger foreshock ion currents and larger electric fields mean that there will be a larger energy transfer from the foreshock ions to the solar wind ions' expansion energy.

As foreshock ions cross the discontinuity, part of their initial parallel and perpendicular speeds project to the new perpendicular direction, which leads to the generation of the current. Therefore, higher initial thermal speeds and parallel speeds can directly increase the partial

gyration speeds and current strengths, which lead to faster expansions. Additionally, the higher thermal speeds give larger gyroradii, which allows the foreshock ions to cross the TD more easily and penetrate farther into the upstream region. This results in a higher total number of partially-gyrating foreshock ions, a stronger current, and therefore more energy transfer to the solar wind ions.

Furthermore, judging by the fitted slopes, m, of the thermal and parallel speeds with the expansion speeds (blue values at the top left of Figures 5b and 5c), the foreshock ion thermal speeds have a stronger influence on the expansion speeds than the foreshock ion parallel speeds. Because the foreshock ion parallel speeds can also affect when the foreshock ions arrive at a fixed position and thus when the structures start to form, we rule out this effect by measuring the expansion speeds at fixed times, relative to their arrival times. We discover that there is also a positive and linear correlation between the foreshock ion parallel speeds and the expansion speeds (Figure S3 in the Supporting Information). In addition, we test the effect of temperature anisotropies and find that increasing the perpendicular temperatures lead to increases in the expansion speeds whereas varying parallel temperatures do not lead to any noticeable differences in the expansion speeds.

Lastly, there are intercepts in Figure 5, i.e., simulation cases with foreshock ion density ratios less than 2%, foreshock ion thermal speeds less than 2 $V_A$, and foreshock ion parallel speeds less than 6 $V_A$ show little formation. This suggests that there are minimum requirements for the foreshock ion parameters to form an FB, i.e., formation criteria. In the accompanying paper (Liu et al., 2023), we fit our simulations with a model equation to further quantify these requirements.

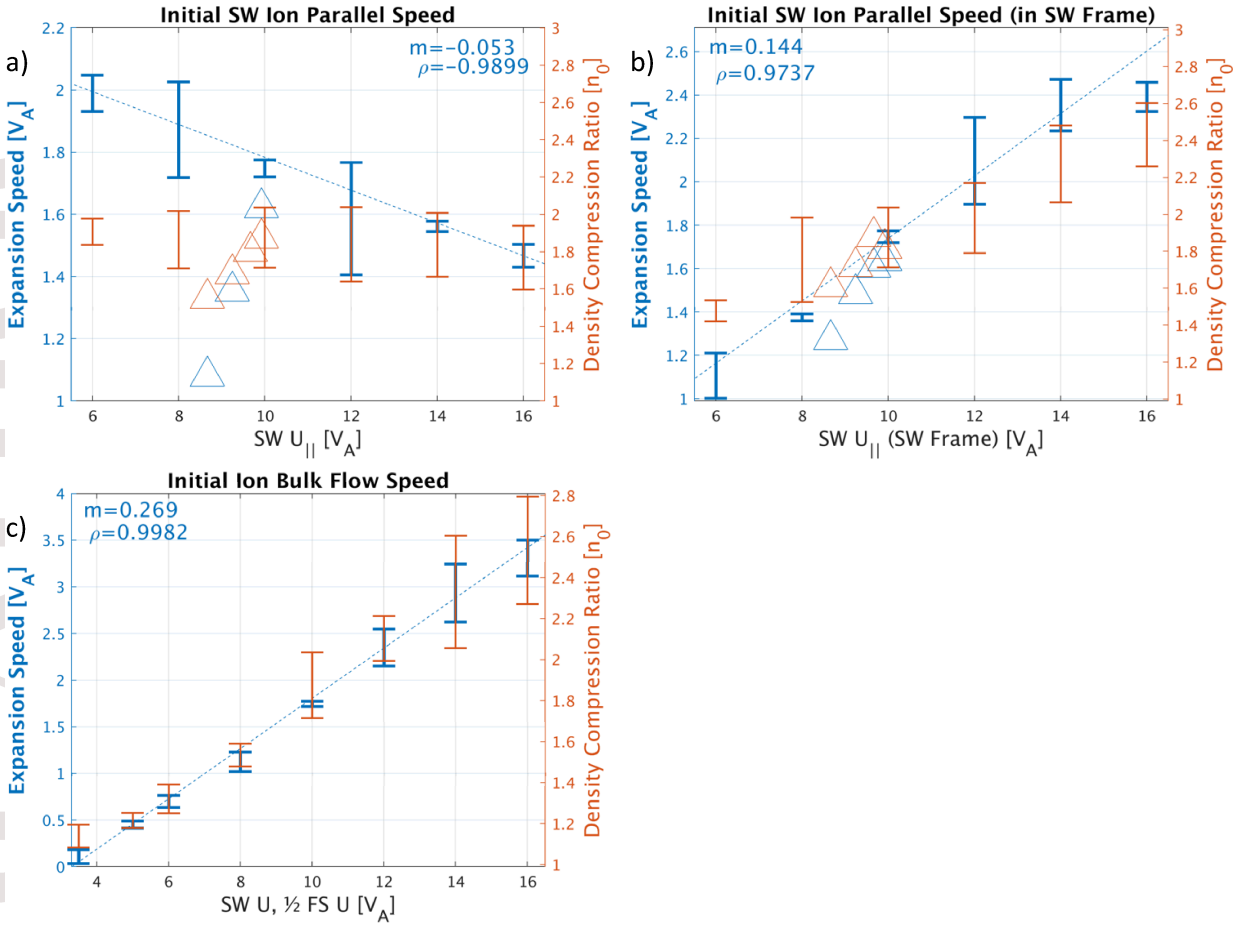


**Figure 6** The solar wind ion parameters' dependencies of the expansion speeds (blue) and density compression ratios (orange) of the compressional boundary at the early stage of formation measured at x=120 $\lambda_i$ and t=6 $\omega_{ci}^{-1}$. The parameters of the initial solar wind parallel speeds (where the foreshock ion speeds are kept constant) for a fixed position and time in panel a), and for a fixed time but different x-positions convecting with the solar wind (same x-positions in the solar wind rest frame) in panel b). Panel c) shows the initial ion bulk flow speeds (where the foreshock ion speeds are adjusted to be twice the solar wind bulk flows, accordingly). The values in blue at the top left of each panel indicate the fitted slope, m, and correlation coefficient, $\rho$, for each parameter with the expansion speeds. The triangles in panels a) and b) are the values for cone angles of 7.5°,15.0°, 22.5°, and 30.0° in the downstream region while the total solar wind speed is 10 $V_A$ and the magnetic shear angle is 90°.

The solar wind ion parameters also play a role in determining the expansion speeds of the structures. In Figure 6a, the solar wind parallel speeds show a negative, though a smaller slope

compared to that of the foreshock ions case, effect on the growth of the structures. This anti-correlation is because as the structures expand, they are also swept, or convected by the solar wind towards the shock (right side of the simulation box). In observations, a foreshock transient typically exhibits weaker structures farther away from the bow shock; therefore, in simulations, at a fixed position, faster convection causes the measurement of weaker structures. To circumvent this issue, Figure 6b shows the relationship between the initial solar wind speeds with the expansion speeds measured at a position convecting with the solar wind. In the solar wind rest frame, the measured expansion speeds positively correlate with the solar wind speeds, as higher solar wind speeds result in larger speed differences between foreshock ion partial gyrations and electrons (thereby generating a stronger current).

To further test the effects of varying solar wind ion parallel speeds, we add a $B_y$ component to the magnetic field that reduces the solar wind ion parallel speeds (foreshock ions remain field-aligned). Because the solar wind ions are always moving in the +x direction, we define the cone angle of 0° to be the instance where the magnetic field is exactly parallel with the solar wind ion bulk flow, in the +x direction. Cone angles above 0° yields lower solar wind ion parallel speeds. Marked as triangles, Figure 6a shows the cases with magnetic field cone angles of 7.5°,15.0°, 22.5°, and 30.0° in the downstream region while keeping the total solar wind speed (10 $V_A$) and TD magnetic shear angle (90°) constant. There is a positive correlation between the higher expansion speeds and smaller cone angles, or larger solar wind ion parallel speeds. This can be explained as follows. For the same total solar wind speed, the convection effect is the same, regardless of the cone angles or the projections of the total solar wind speeds in the parallel direction. But as the cone angles increase, the relative parallel speeds between the solar wind ions and the field-aligned foreshock ions decrease. As a result, for the same total solar wind ion speed, increasing the cone angles will yield smaller expansion speeds.

To exclude the convection effect, Figure 6b shows the expansion speeds with measurement position following the solar wind. As expected, the expansion speeds are now positively correlated with the solar wind speeds. For the cone angle cases, however, the slope is steeper. One possible reason is the time-of-flight effect where faster (and colder) foreshock ions travel farther away, resulting in a dispersion. When the cone angle is larger, the distance along the field line to the same x-position is longer, which causes a stronger time-of-flight effect; we do see that the local background foreshock ions are faster and colder for the larger cone angle cases (not shown).

Furthermore, because the expansion speeds of FBs have a stronger dependence on the foreshock ion thermal speeds than the parallel speeds (Figure 5), the local structure is thus even weaker for cases with larger cone angles.

In Figure 6c, when the foreshock ion speeds are increased alongside the solar wind ion speeds (foreshock ion speeds are twice in magnitude of the solar wind ion speeds), then there is a positive and linear correlation between the expansion speeds and the density compression ratios measured at a fixed position in the simulation rest frame. With regards to the expansion speeds, though there is a negative correlation with increasing the solar wind parallel speeds (Figure 6a), there is a much stronger positive correlation with increasing the foreshock ion parallel speeds (Figure 5c) that overcomes the convection effect and favors higher expansion speeds (which can also be seen by their slopes).

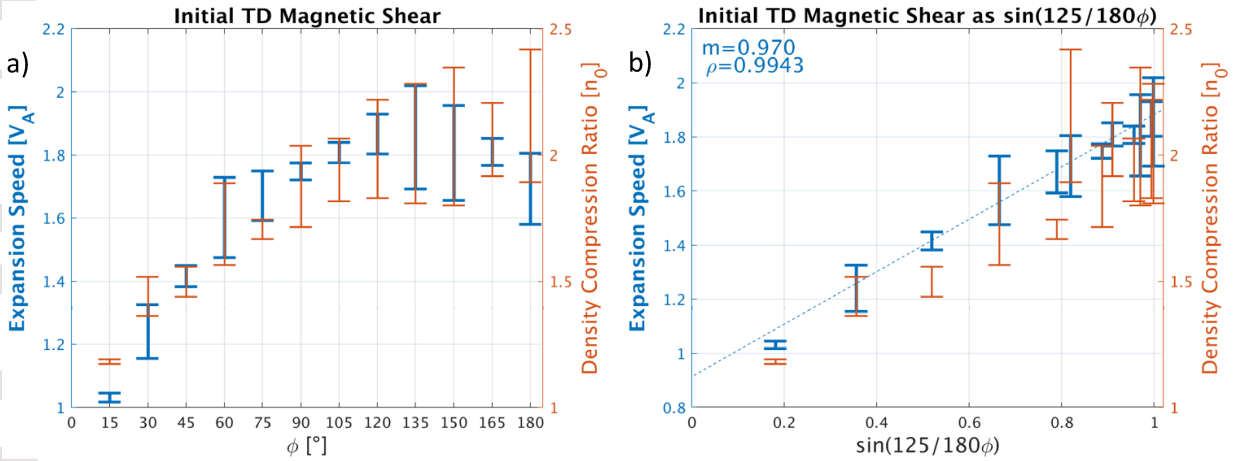


**Figure 7** The TD magnetic shear angles' dependencies of the expansion speeds (blue) and density compression ratios (orange) of the compressional boundary at the early stage of formation measured at x=120 $\lambda_i$ and t=6 $\omega_{ci}^{-1}$. Panels a) to b) show the parameters of the initial TD magnetic shear angle and the sin of TD magnetic shear angle multiplied by a best-fit constant of 125/180. The values in blue at the top left of panel b) indicate the fitted slope, m, and correlation coefficient, $\rho$, for sin(125/180$\phi$) with the expansion speeds.

From Vu et al. (2022), it is shown that how much magnetic shear foreshock ions experience within their gyromotion at the TD affects the relative strengths of the generated currents at the TD. Therefore, we explore the TD magnetic shear dependence on the growth of the compressional boundary of FBs by varying the magnetic shear of TDs between 15° to 180° (by changing the upstream magnetic field directions). Figure 7a shows the expansion speeds increase for higher

magnetic shear angles until angles between 120° to 135°, after which the expansion speeds begin to decrease. However, the density compressions do not follow the same trend and continue to increase beyond this range of critical shear angles (possibly related to other FB shock parameters, such as $\theta_{Bn}$). This critical shear angle range alludes to previous observational statistical studies done by, e.g., Schwartz et al. (2000), Facskó et al. (2008, 2009, 2010), Zhao et al. (2017), Liu et al. (2021), and Vu et al. (2022), where increasing magnetic shear angles up until a cutoff shear angle of around 120° favor the occurrence for both FBs and HFAs. In Figure 7b, we find that $\sin(125/180\phi)$ best fits the magnetic shear angles, $\phi$, to a function that allows it to be more linearly correlated with the expansion speeds. With this function, the expansion speeds increase linearly up to $\phi = 125°$, after which the expansion speeds decrease linearly. A possible reason is that as the FB forms, the magnetic field profile is modified around the TD; therefore, the foreshock ions can only experience a fraction of the initial magnetic shear angle of the TD. And the sine may come from the projection of the initial parallel velocity of foreshock ions into the new perpendicular direction. From our results, this fraction of the initial magnetic shear that the foreshock ions experience appears to be a constant, regardless of the initial shear angle. Therefore, we suspect this fraction could be a function of other parameters. Another possibility is that a higher shear angle may cause a stronger projection into the perpendicular direction from the initial perpendicular speed. Although the foreshock ions are initially gyrotropic, as only a certain gyrophase range of foreshock ions can cross the TD, the perpendicular speed can still contribute. Higher shear angles favor a smaller gyrophase range and thus a larger gyrophase-averaged perpendicular bulk velocity. The role of the shear angle needs further tests in the future.

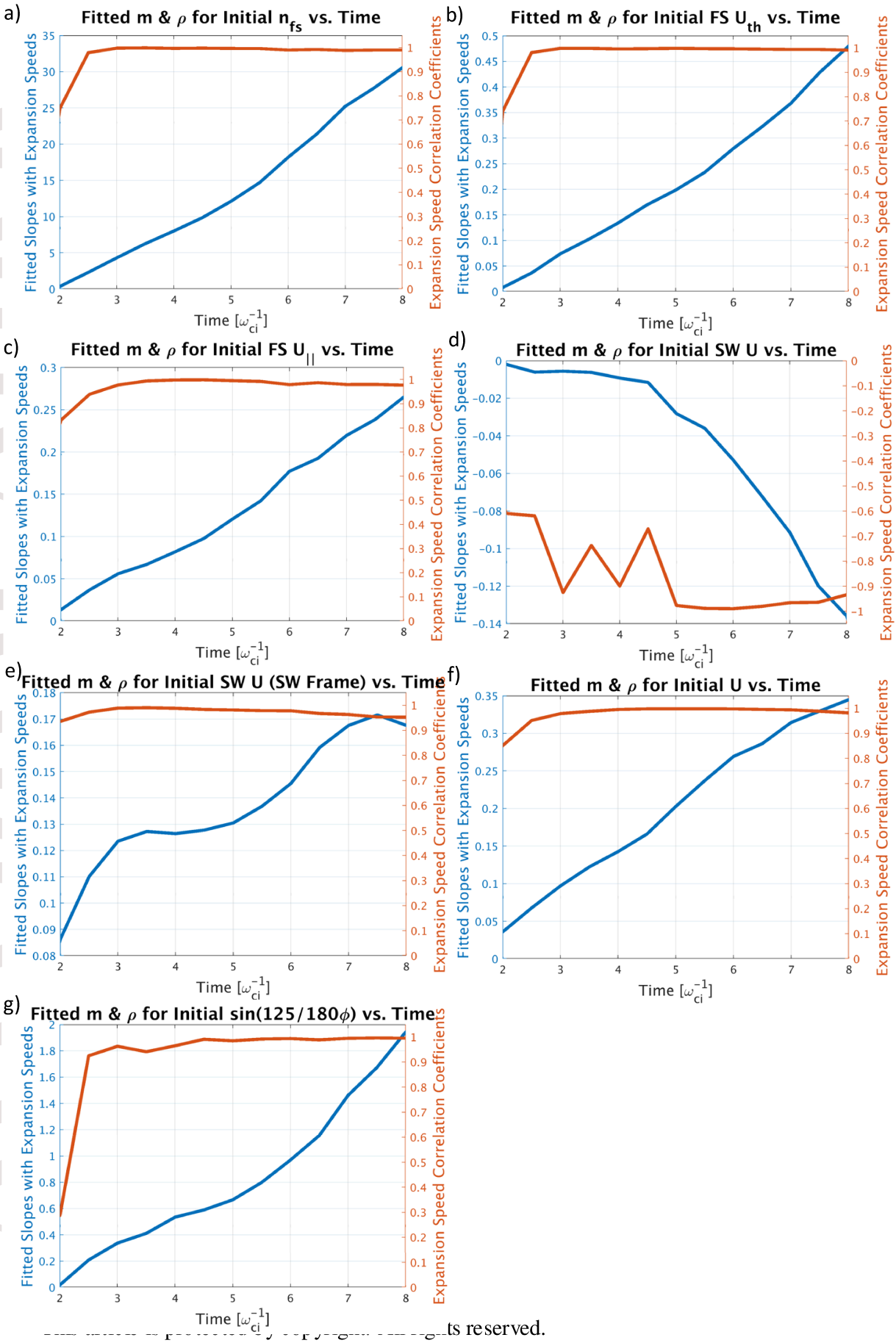

**Figure 8** The fitted slopes (blue) and the correlation coefficients (orange) for the parameter dependencies over time. Panels a) to g) show the parameters of foreshock ion densities, foreshock ion thermal speeds, foreshock ion parallel speeds, solar wind parallel speeds, solar wind parallel speeds in the solar wind rest frame, solar wind and foreshock ion bulk flows, and sin(125/180$\phi$), where $\phi$ is the magnetic shear angles of the TDs.

During the early stages of formation, the effects of foreshock ion parameter dependencies of the expansion speeds vary with time. Figure 8 shows how the slopes and the correlation coefficients for each parameter evolve with time. For all quantities, the magnitudes of the fitted slopes increase over time and the correlation coefficients are maintained near 1.0 (or -1.0 for the solar wind ion parallel speeds) during the early formation. In other words, increasing the foreshock ion densities, foreshock ion thermal speeds, foreshock ion parallel speeds, solar wind ion parallel speeds in the solar wind rest frame, solar wind and foreshock ion bulk flows, and the TD magnetic shear angles in sin(125/180$\phi$) have a positive influence on the early formation of structures throughout the formation time scale, and their effects on the expansion speeds grow in strength over time. The reason for the growing effects is discussed by the model in the accompanying paper (Liu et al., 2023). In Figure 8d of the solar wind ion parallel speeds, the negative correlation with the measured expansion speeds is consistent for all times, and the negative contribution to the measured expansion speeds is also intensified over time (partly due to the FB shock normal pointing more sunward over time). At early times, the slopes are flat, and the correlation coefficients fluctuate. This is because, for very fast solar wind speeds, the formed structures are easily convected towards the "bow shock" and hardly reach the fixed measurement position at early times, thus the measured expansion speeds are rather noisy and do not fit the trend set by those for slow solar wind speeds.

# 4 Discussion

The study presented in this paper reconfirms the kinetic formation model of TD-driven FBs through the interactions of foreshock ions at the TD. Foreshock ions perform partial gyrations at the TD to generate currents that change the magnetic field of the TD. By varying the distributions of the injected foreshock ions, we find that the profile of the foreshock ion distribution in the

perpendicular plane decides whether and how easily the foreshock ions can cross the TD and determines the extent of their perpendicular speeds that get projected. This, in turn, dictates the strength of the foreshock ion-driven current that decides the extent of the density variation of the structure. Our results show that the initial gyrophase of the gyrophase-bunched distribution is critical to the early formation of foreshock transients, agreeing with the global hybrid simulations in Lin et al. (2022). From Table 1, when the foreshock ions are injected as a gyrophase bunched distribution with gyrocenters upstream of the TD or injected as a ring beam (both cases with comparable initial perpendicular energies), their resultant density profiles (consisting of the core and the compressional boundary) show more significant variations than those when the foreshock ions are injected as a Maxwellian beam. We also see that these non-Maxwellian distributions also have faster boundary speeds, or expansion speeds, of the structures.

**Table 1**. Initial injected foreshock ion distributions and their TD-driven FB properties at t=6 $\omega_{ci}^{-1}$

| **Foreshock ion distribution** | **Initial foreshock ion $E_\perp$ ($E_{\perp,Maxw}$)** | **Core density ($n_0$)** | **Boundary density ($n_0$)** | **Boundary $V_z$ ($V_A$)** | **FB Shock Speed ($V_A$)** |
|---|---|---|---|---|---|
| **Maxwellian beam** | 1.0 | 0.57 | 1.71 | 1.1 | 2.6 |
| **Gyrophase-bunched** (gyrocenter above TD) | 0.8 | 0.18 | 3.35 | 2.8 | 4.0 |
| **Gyrophase-bunched** (gyrocenter below TD) | 0.8 | 0.85 | 1.23 | 0.1 | 0.5 |
| **Ring beam** (ring speed $\sqrt{\mathbf{48}}$ $V_A$) | 1.0 | 0.30 | 2.45 | 2.2 | 3.7 |
| **Ring beam** (ring speed 8 $V_A$) | 2.0 | 0.28 | 2.65 | 2.5 | 4.0 |

As for the differences among the same foreshock ion distributions, the phase which has the guiding center on the other (upstream) side of the TD (Figure 2) provided for the strongest growth by causing most of the foreshock ions to gyrate across the TD. On the contrary, the phase which has the guiding center on the same side away (downstream) from the TD (Figure 3) provided

for the weakest growth. When all the injected foreshock ions have an initial gyrophase that is directed away from the TD (shown in Figure S1 in the Supporting Information), then the resultant signatures lie somewhere in between the two gyrophases. This intermediate gyrophase also yields more significant signatures than those of the Maxwellian beam. As for the case of the ring distribution, the ring beam (Figure 4), with the same perpendicular energy as the Maxwellian beam case, can project more of its speed into the new perpendicular direction, and acquire larger gyroradii, resulting in a stronger current. Thus, there is a lower depletion within the core and a higher compression at the boundary, as well as a faster expansion speed. With a higher ring speed and perpendicular energy, the effect is amplified, as shown in Figure S2 in the Supporting Information.

Therefore, in future studies, we plan to continue our study of gyrophase-bunched and ring beam distributions by varying the initial parameters of the distribution. Specifically, it would reveal the relative influences of the parameters, such as the initial thermal speeds, initial gyrophases, or additional perpendicular bulk flow speeds, on the early formation of the TD-driven FBs.

**Table 2**. Varied initial simulation parameters and fitted slopes with expansion speeds at t=6 $\omega_{ci}^{-1}$

| **Varied initial simulation parameters** | **Fitted slopes of expansion speeds vs. parameter values** |
|---|---|
| **Foreshock ion density** | 18.5 $V_A/n_0$ |
| **Foreshock ion thermal speed** | 0.28 $V_A/V_A$ |
| **Foreshock ion parallel speed** | 0.18 $V_A/V_A$ |
| **Solar wind ion parallel speed (shock frame)** | -0.50 $V_A/V_A$ |
| **Solar wind ion parallel speed (solar wind frame)** | 0.14 $V_A/V_A$ |
| **Solar wind and foreshock ion parallel speed (shock frame)** | 0.27 $V_A/V_A$ |
| **sin(125/180 TD magnetic shear angle)** | 0.97 $V_A$/# |

By varying the parameters of the injected Maxwellian beam of foreshock ions, we also discover that parameters that increase how many foreshock ions cross the TD, such as the foreshock ion densities, thermal speeds, and parallel speeds, cause faster expansions of the structures. In addition, higher solar wind ion parallel speeds and TD magnetic shear angles (up to

120º) lead to faster expansion speeds of the structures. From Table 2 of the fitted slopes of the expansion speeds vs. the parameter values, most of the studied parameters positively and linearly correlate with the expansion speeds and the density compression ratios of the formed structures. The reason is that these parameters either allow more foreshock ions to cross the TD or allow foreshock ions to project higher perpendicular speeds across the TD, which results in larger currents and ultimately higher expansion speeds for the TD-driven FBs. Moreover, we also find that increasing the thermal speeds of foreshock ions has a much stronger effect on increasing the expansion speeds than increasing the parallel speeds of foreshock ions. Keeping track of the relationship between the expansion speeds and these parameters throughout the simulation times, we find that the studied foreshock ion parameters' effect on the expansion speeds of the structures grows in magnitude as the simulation proceeds during the early formation stages. As for modeling the expansion speed of foreshock bubbles, there is also a multi-variable fitting on a physics-based equation demonstrated in the accompanying paper by Liu et al., (2023).

In this paper, we have shown that increasing the magnetic shear angles up to 120° of the driver TD produces more significant structures, but we have not explored the effects of different thicknesses and orientations of the driver discontinuity. From earlier work, Vu et al. (2022) have shown the differences between a thin and a thick TD in forming TD-driven FBs and HFAs; therefore, it is necessary to perform a parameter scan of the intermediate TD thicknesses to quantitatively study how they alter the strengths of the foreshock-driven currents, compression ratios of the compressional boundaries, and expansion speeds of TD-driven FBs. Furthermore, from previous statistical studies (e.g., Schwartz et al., 2000; Facskó et al., 2008, 2009, 2010; Liu et al., 2021), the orientation of the TD relative to the shock normal also plays a role in the early formation of the structures. Thus, to better understand their impacts on the early formation of foreshock transients, additional parameter scans of varying TD properties will be investigated in future simulation work.

In addition, a recent statistical study by Liu et al. (2022) shows that larger density ratios and higher kinetic energies of the foreshock ions favor the formation of FBs and HFAs, consistent with our simulation results. As for the thermal speed, however, Liu et al. (2022) show that a larger gyroradius calculated from the perpendicular thermal speed is a favorable condition, instead of the thermal speed. It is more likely the foreshock ion gyroradius relative to the discontinuity parameters that determines the early formation; but this requires further tests in the future.

For the simplicity of understanding the underlying mechanisms, we use local hybrid simulations with fine-tuned parameters to demonstrate the kinetic formation model involving foreshock ions interacting with a discontinuity. By injecting constant foreshock ion distributions at all space and times, we can pinpoint the exact processes that lead to the early formation of the structures. However, in nature, the foreshock ion distributions and properties are far more complex in the environments around a real bow shock (e.g., curvature, ripples, and reformation). Foreshock ions generated at the bow shock, either from adiabatic reflection, specular reflection, or pickup, can all possess complicated ion distributions and properties that vary spatially and temporally. Therefore, global hybrid simulations can be used to understand the early formation and evolution of foreshock transients in more realistic curved shock environments.

Lastly, our hybrid simulations only showcase the different foreshock ion distributions and varying foreshock ion properties' influence on the early formation of TD-driven FBs. For future studies, it would also be important to understand how these parameters affect the early formation of HFAs with two compressional boundaries. Namely, how the foreshock ion properties affect the relative compression ratios and the expansion speeds of each of the two boundaries in HFAs. In addition, our simulations only inject the foreshock ions on one side of the TD. In many situations, as seen in spacecraft observations of HFAs, for example, foreshock ions are observed on both sides of the TD, i.e., a TD embedded within the ion foreshock. Additionally, similar studies for rotational discontinuity cases are also needed.

# 5 Conclusions

Using 2-D local hybrid simulations of different foreshock ion distributions and different foreshock ion, solar wind ion, and TD properties, we study their effects on the early formation and expansion of TD-driven FBs. The study reconfirms the kinetic formation model for the early formation of discontinuity-driven foreshock transients where foreshock ions at the TD perform partial gyrations to generate currents that change the magnetic field of the TD. The study uncovered the following:

- The shape of the foreshock ion distribution in the perpendicular plane determines how easily the foreshock ions can cross the TD and then subsequently generate currents.

- Foreshock ion parameters, such as the initial densities, thermal speeds, and parallel speeds all positively and linearly correlate with the expansion speeds and density compression ratios of the upstream compressional boundaries of FBs.
- The TD magnetic shears positively correlate with the expansion speeds and density compression ratios up to 120 degrees, and the dependence can be fitted into a function, $\sin(125/180\phi)$.
- These parameter dependencies on the expansion speeds of the structures grow with time.
- When there is a higher density of foreshock ions across the TD or when the foreshock ions have higher perpendicular speeds, or larger gyroradii, at the TD, then they can generate stronger currents, cause more significant field variations, and yield faster expansion speeds for the TD-driven FBs.

In all, the study does elucidate more on the kinetic formation model by revealing the impact of different injected foreshock ion properties on the expansion of TD-driven FBs in their early formation stages. This work also helps quantify the role of these parameters as shown in the accompanying paper (Liu et al., 2023); however, there is still much to uncover about the formation of these structures at later stages and in real shock environments. Furthermore, foreshock transients are known to cause many space weather effects and increase shock acceleration efficiency. This work improves our understanding of the formation process and provides a dataset to establish a predictive model of foreshock transients to forecast their space weather effects and to determine their role in shock physics in general.

## Acknowledgments

This work is supported by NSF AGS-1352669 and NASA grant 80NSSC18K1376. T. Z. L. is partially supported by NSF award AGS-1941012, NASA grant 80NSSC21K1437, and NASA grant 80NSSC23K0086. This work was supported in part by the high-performance computing and data storage resources operated by the Research Computing Systems Group at the University of Alaska Fairbanks Geophysical Institute.

## Open Research

The simulation data used for the figures and analysis in the study are available at https://doi.org/10.6084/m9.figshare.20208899.v1.

# References


An, X., Liu, T. Z., Bortnik, J., Osmane, A., & Angelopoulos, V. (2020). Formation of Foreshock Transients and Associated Secondary Shocks. *The Astrophysical Journal*, *901*(1). https://doi.org/10.3847/1538-4357/abaf03

Archer, M. O., Turner, D. L., Eastwood, J. P., Horbury, T. S., & Schwartz, S. J. (2014). The role of pressure gradients in driving sunward magnetosheath flows and magnetopause motion. *Journal of Geophysical Research: Space Physics*, *119*(10), 8117–8125. https://doi.org/10.1002/2014JA020342

Archer, M. O., Turner, D. L., Eastwood, J. P., Schwartz, S. J., & Horbury, T. S. (2015). Global impacts of a Foreshock Bubble: Magnetosheath, magnetopause and ground-based observations. *Planetary and Space Science*, *106*, 56–66. https://doi.org/10.1016/j.pss.2014.11.026

Chu, C., Zhang, H., Sibeck, D., Otto, A., Zong, Q., Omidi, N., McFadden, J. P., Fruehauff, D., & Angelopoulos, V. (2017). THEMIS satellite observations of hot flow anomalies at Earth's bow shock. *Annales Geophysicae*, *35*(3). https://doi.org/10.5194/angeo-35-443-2017

Delamere, P. A. (2009). Hybrid code simulations of the solar wind interaction with Pluto. *Journal of Geophysical Research: Space Physics*, *114*(3). https://doi.org/10.1029/2008JA013756

Delamere, P. A. (2006). Hybrid code simulations of the solar wind interaction with Comet 19P/Borrelly. *Journal of Geophysical Research*, *111*(A12). https://doi.org/10.1029/2006JA011859

Delamere, P. A., Swift, D. W., & Stenbaek-Nielsen, H. C. (1999). A three-dimensional hybrid code simulation of the December 1984 solar wind AMPTE release. *Geophysical Research Letters*, *26*(18), 2837–2840. https://doi.org/10.1029/1999GL900602

Facskó, G., Kecskeméty, K., Erdős, G., Tátrallyay, M., Daly, P. W., & Dandouras, I. (2008). A statistical study of hot flow anomalies using Cluster data. *Advances in space research*, *41*(8), 1286-1291.

Facskó, G., Nemeth, Z., Erdős, G., Kis, A., & Dandouras, I. (2009). A global study of hot flow anomalies using Cluster multi-spacecraft measurements. In *Annales geophysicae* (Vol. 27, No. 5, pp. 2057-2076). Copernicus GmbH.

Facskó, G., Trotignon, J. G., Dandouras, I., Lucek, E. A., & Daly, P. W. (2010). Study of hot flow anomalies using Cluster multi-spacecraft measurements. *Advances in space research*, *45*(4), 541-552.

Hartinger, M. D., Turner, D. L., Plaschke, F., Angelopoulos, V., & Singer, H. (2013). The role of transient ion foreshock phenomena in driving Pc5 ULF wave activity. *Journal of Geophysical Research: Space Physics*, *118*(1), 299–312. https://doi.org/10.1029/2012JA018349

Helder, E. A., Vink, J., Bykov, A. M., Ohira, Y., Raymond, J. C., & Terrier, R. (2012). Observational signatures of particle acceleration in supernova remnants. In *Space Science Reviews* (Vol. 173, Issues 1–4, pp. 369–431). https://doi.org/10.1007/s11214-012-9919-8

Jacobsen, K. S., Phan, T. D., Eastwood, J. P., Sibeck, D. G., Moen, J. I., Angelopoulos, V., McFadden, J. P., Engebretson, M. J., Provan, G., Larson, D., & Fornaçon, K. H. (2009). THEMIS observations of extreme magnetopause motion caused by a hot flow anomaly. *Journal of Geophysical Research: Space Physics*, *114*(8), 1–10. https://doi.org/10.1029/2008JA013873

Kecskeméty, K., Erdős, G., Facskó, G., Tátrallyay, M., Dandouras, I., Daly, P., & Kudela, K. (2006). Distributions of suprathermal ions near hot flow anomalies observed by RAPID aboard Cluster. *Advances in Space Research*, *38*(8), 1587-1594.

Lee, M. A., Mewaldt, R. A., & Giacalone, J. (2012). Shock acceleration of ions in the heliosphere. In *Space Science Reviews* (Vol. 173, Issues 1–4, pp. 247–281). https://doi.org/10.1007/s11214-012-9932-y

Liu, T. Z., An, X., Zhang, H., & Turner, D. (2020b). Magnetospheric Multiscale Observations of Foreshock Transients at Their Very Early Stage. *The Astrophysical Journal*, *902*(1). https://doi.org/10.3847/1538-4357/abb249

Liu, T. Z., Angelopoulos, V., Hietala, H., & Wilson III, L. B. (2017a). Statistical study of particle acceleration in the core of foreshock transients. *Journal of Geophysical Research: Space Physics*, *122*(7). https://doi.org/10.1002/2017JA024043

Liu, T. Z., Angelopoulos, V., & Lu, S. (2019). Relativistic electrons generated at Earth's quasi-parallel bow shock. *Science Advances*, *5*(7). https://doi.org/10.1126/sciadv.aaw1368

Liu, T. Z., Hietala, H., Angelopoulos, V., & Turner, D. L. (2016b). Observations of a new foreshock region upstream of a foreshock bubble's shock. *Geophysical Research Letters*, *43*(10). https://doi.org/10.1002/2016GL068984

Liu, T. Z., Zhang, H., Turner, D., Vu, A., & Angelopoulos, V. (2022). Statistical study of favorable foreshock ion properties for the formation of hot flow anomalies and foreshock bubbles. Journal of Geophysical Research: Space Physics, 127, e2022JA030273. https://doi.org/10.1029/2022JA030273

Liu, T. Z., Lu, S., Angelopoulos, V., Hietala, H., & Wilson, L. B. (2017b). Fermi acceleration of electrons inside foreshock transient cores. *Journal of Geophysical Research: Space Physics*, *122*(9). https://doi.org/10.1002/2017JA024480

Liu, T. Z., Lu, S., Angelopoulos, V., Lin, Y., & Wang, X. Y. (2018). Ion Acceleration Inside Foreshock Transients. *Journal of Geophysical Research: Space Physics*, *123*(1). https://doi.org/10.1002/2017JA024838

Liu, T. Z., Lu, S., Turner, D. L., Gingell, I., Angelopoulos, V., Zhang, H., Artemyev, A., & Burch, J. L. (2020a). Magnetospheric Multiscale (MMS) Observations of Magnetic Reconnection in Foreshock Transients. *Journal of Geophysical Research: Space Physics*, *125*(4). https://doi.org/10.1029/2020JA027822

Liu, T. Z., Turner, D. L., Angelopoulos, V., & Omidi, N. (2016a). Multipoint observations of the structure and evolution of foreshock bubbles and their relation to hot flow anomalies. *Journal of Geophysical Research: Space Physics*, *121*(6). https://doi.org/10.1002/2016JA022461

Liu, T. Z., A. Vu, H. Zhang, X. An, and V. Angelopoulos (2023). Modeling the expansion speed of foreshock bubbles, accepted to JGR (Manuscript Sent to Production)

Liu, T. Z., Zhang, H., Wang, C. P., Angelopoulos, V., Vu, A., Wang, X., & Lin, Y. (2021). Statistical Study of Foreshock Transients in the Midtail Foreshock. *Journal of Geophysical Research: Space Physics*, *126*(5). https://doi.org/10.1029/2021JA029156

Liu, Z., Turner, D. L., Angelopoulos, V., & Omidi, N. (2015). THEMIS observations of tangential discontinuity-driven foreshock bubbles. *Geophysical Research Letters*, *42*(19). https://doi.org/10.1002/2015GL065842

Lucek, E. A., Horbury, T. S., Balogh, A., & Dandouras, I. (2004). Cluster observations of hot flow anomalies. *Journal of Geophysical Research*, *109*(A6). https://doi.org/10.1029/2003JA010016

Omidi, N., Eastwood, J. P., & Sibeck, D. G. (2010). Foreshock bubbles and their global magnetospheric impacts. *Journal of Geophysical Research: Space Physics*, *115*(A6). https://doi.org/10.1029/2009JA014828

Omidi, N., Lee, S. H., & Sibeck, D. G. (2021). Ion Acceleration by Foreshock Bubbles. *Journal of Geophysical Research: Space Physics*, *126*(5), 1–17. https://doi.org/10.1029/2020JA028924

Omidi, N., Lee, S. H., Sibeck, D. G., Turner, D. L., Liu, T. Z., & Angelopoulos, V. (2020). Formation and Topology of Foreshock Bubbles. *Journal of Geophysical Research: Space Physics*, *125*(9). https://doi.org/10.1029/2020JA028058

Paschmann, G., Haerendel, G., Sckopke, N., Möbius, E., Lühr, H., & Carlson, C. W. (1988). Three-dimensional plasma structures with anomalous flow directions near the Earth's bow shock. *Journal of Geophysical Research*, *93*(A10). https://doi.org/10.1029/JA093iA10p11279

Schwartz, S. (1995). Hot flow anomalies near the Earth's bow shock. *Advances in Space Research*, *15*(8–9). https://doi.org/10.1016/0273-1177(94)00092-F

Schwartz, S. J., Avanov, L., Turner, D., Zhang, H., Gingell, I., Eastwood, J. P., Gershman, D. J., Johlander, A., Russell, C. T., Burch, J. L., Dorelli, J. C., Eriksson, S., Ergun, R. E., Fuselier, S. A., Giles, B. L., Goodrich, K. A., Khotyaintsev, Y. V, Lavraud, B., Lindqvist, P., … Wilder, F. (2018). Ion Kinetics in a Hot Flow Anomaly: MMS Observations. *Geophysical Research Letters*, *45*(21). https://doi.org/10.1029/2018GL080189

Schwartz, S. J., Chaloner, C. P., Christiansen, P. J., Coates, A. J., Hall, D. S., Johnstone, A. D., Gough, M. P., Norris, A. J., Rijnbeek, R. P., Southwood, D. J., & Woolliscroft, L. J. C. (1985). An active current sheet in the solar wind. *Nature*, *318*(6043). https://doi.org/10.1038/318269a0

Schwartz, S. J., Paschmann, G., Sckopke, N., Bauer, T. M., Dunlop, M., Fazakerley, A. N., & Thomsen, M. F. (2000). Conditions for the formation of hot flow anomalies at Earth's bow shock. *Journal of Geophysical Research: Space Physics*, *105*(A6). https://doi.org/10.1029/1999JA000320

Sibeck, D. G., Borodkova, N. L., Schwartz, S. J., Owen, C. J., Kessel, R., Kokubun, S., Lepping, R. P., Lin, R., Liou, K., Lühr, H., McEntire, R. W., Meng, C.-I., Mukai, T., Nemecek, Z., Parks, G., Phan, T. D., Romanov, S. A., Safrankova, J., Sauvaud, J.-A., … Zastenker, G. N. (1999). Comprehensive study of the magnetospheric response to a hot flow anomaly. *Journal of Geophysical Research: Space Physics*, *104*(A3). https://doi.org/10.1029/1998JA900021

Swift, D. W. (1995). Use of a hybrid code to model the Earth's magnetosphere. *Geophysical Research Letters*, *22*(3). https://doi.org/10.1029/94GL03082

Swift, D. W. (1996). Use of a Hybrid Code for Global-Scale Plasma Simulation. *Journal of Computational Physics*, *126*(1). https://doi.org/10.1006/jcph.1996.0124

Thomsen, M. F., Gosling, J. T., Fuselier, S. A., Bame, S. J., & Russell, C. T. (1986). Hot, diamagnetic cavities upstream from the Earth's bow shock. *Journal of Geophysical Research*, *91*(A3). https://doi.org/10.1029/JA091iA03p02961

Turner, D. L., Liu, T. Z., Wilson, L. B., Cohen, I. J., Gershman, D. G., Fennell, J. F., Blake, J. B., Mauk, B. H., Omidi, N., & Burch, J. L. (2020). Microscopic, Multipoint Characterization of Foreshock Bubbles With Magnetospheric Multiscale (MMS). *Journal of Geophysical Research: Space Physics*, *125*(7). https://doi.org/10.1029/2019JA027707

Turner, D. L., Omidi, N., Sibeck, D. G., & Angelopoulos, V. (2013). First observations of foreshock bubbles upstream of Earth's bow shock: Characteristics and comparisons to HFAs. *Journal of Geophysical Research: Space Physics*, *118*(4). https://doi.org/10.1002/jgra.50198

Vu, A., Liu, T. Z., Zhang, H., & Delamere, P. (2022). Hybrid simulations of a tangential discontinuity-driven foreshock bubble formation in comparison with a hot flow anomaly formation. *Journal of Geophysical Research: Space Physics*, *127*, e2021JA029973. https://doi. org/10.1029/2021JA029973

Wang, B., Liu, T., Nishimura, Y., Zhang, H., Hartinger, M., Shi, X., Ma, Q., Angelopoulos, V., & Frey, H. U. (2020). Global Propagation of Magnetospheric Pc5 ULF Waves Driven by Foreshock Transients. *Journal of Geophysical Research: Space Physics*, *125*(12), 1–20. https://doi.org/10.1029/2020JA028411

Wang, B., Zhang, H., Liu, Z., Liu, T., Li, X., & Angelopoulos, V. (2021). Energy Modulations of Magnetospheric Ions Induced by Foreshock Transient-Driven Ultralow-Frequency Waves. *Geophysical Research Letters*, *48*(10), 1–11. https://doi.org/10.1029/2021GL093913

Wang, C. P., Wang, X., Liu, T. Z., & Lin, Y. (2021b). Impact of Foreshock Transients on the Flank Magnetopause and Magnetosphere and the Ionosphere. *Frontiers in Astronomy and Space Sciences*, *8*(September), 1–17. https://doi.org/10.3389/fspas.2021.751244

Wang, C. P., Wang, X., Liu, T. Z., & Lin, Y. (2021a). A Foreshock Bubble Driven by an IMF Tangential Discontinuity: 3D Global Hybrid Simulation. *Geophysical Research Letters*, *48*(9). https://doi.org/10.1029/2021GL093068

Wang, C. P., Wang, X., Liu, T. Z., & Lin, Y. (2020). Evolution of a Foreshock Bubble in the Midtail Foreshock and Impact on the Magnetopause: 3-D Global Hybrid Simulation. *Geophysical Research Letters*, *47*(22), 1–10. https://doi.org/10.1029/2020GL089844

Wang, S., Zong, Q., & Zhang, H. (2012). Cases and statistical study on Hot Flow Anomalies with Cluster spacecraft data. *Science China Technological Sciences*, *55*(5). https://doi.org/10.1007/s11431-012-4767-z

Wilson, L. B., Sibeck, D. G., Turner, D. L., Osmane, A., Caprioli, D., & Angelopoulos, V. (2016). Relativistic Electrons Produced by Foreshock Disturbances Observed Upstream of Earth's Bow Shock. *Physical Review Letters*, *117*(21). https://doi.org/10.1103/PhysRevLett.117.215101

Lin, Y., Wang, X., Sibeck, D. G., Wang, C.-P., & Lee, S.-H. (2022). Global asymmetries of hot flow anomalies. *Geophysical Research Letters*, 49, e2021GL096970. https://doi.org/10.1029/2021GL096970

Zhang, H., Zong, Q.-G., Connor, H. et al. Dayside transient phenomena and their impact on the magnetosphere and ionosphere. Space Sci Rev (2022). https://doi.org/10.1007/s11214-021-00865-0

Zhao, L. L., Zhang, H., & Zong, Q. G. (2017). A statistical study on hot flow anomaly current sheets. *Journal of Geophysical Research: Space Physics*, *122*(1), 235–248. https://doi.org/10.1002/2016JA023319

Zhao, L. L., Zong, Q. G., Zhang, H., & Wang, S. (2015). Case and statistical studies on the evolution of hot flow anomalies. *Journal of Geophysical Research: Space Physics*, *120*(8). https://doi.org/10.1002/2014JA020862

Meziane, K., Mazelle, C., Wilber, M., LeQuéau, D., Eastwood, J. P., Rème, H., Dandouras, I., Sauvaud, J. A., Bosqued, J. M., Parks, G. K., Kistler, L. M., McCarthy, M., Klecker, B., Korth, A., Bavassano-Cattaneo, M.-B., Lundin, R., and Balogh, A.: Bow shock specularly reflected ions in the presence of low-frequency electromagnetic waves: a case study, Ann. Geophys., 22, 2325–2335, https://doi.org/10.5194/angeo-22-2325-2004, 2004.

Tjulin, A., Lucek, E. A., and Dandouras, I. (2009), Observations and modeling of particle dispersion signatures at a hot flow anomaly, J. Geophys. Res., 114, A06208, doi:10.1029/2009JA014065.

Burgess, D., Möbius, E. & Scholer, M. Ion Acceleration at the Earth's Bow Shock. Space Sci Rev 173, 5–47 (2012). https://doi.org/10.1007/s11214-012-9901-5